Mineral formation in the primary polyps of pocilloporoid corals

Maayan Neder, Pierre Philippe Laissue, Anat Akiva, Derya Akkaynak, Marie
N Albéric, Oliver Spaeker, Yael Politi, Iddo Pinkas, Tali Mass

Full length article

Mineral formation in the primary polyps of pocilloporoid corals

Maayan Neder [a,b], Pierre Philippe Laissue [c], Anat Akiva [d], Derya Akkaynak [b,e], Marie Albéric [f], Oliver Spaeker [f], Yael Politi [f], Iddo Pinkas [g,*], Tali Mass [a,*]

[a] Department of Marine Biology, The Leon H. Charney School of Marine Sciences, University of Haifa, Mt. Carmel, Haifa 3498838, Israel
[b] The Interuniversity Institute of Marine Sciences, Eilat 88103, Israel
[c] School of Biological Sciences, Wivenhoe Park, University of Essex, Colchester CO4 3SQ, UK
[d] Laboratory of Materials and Interface Chemistry and Center for Multiscale Electron Microscopy, Department of Chemical Engineering and Chemistry and Institute for Complex Molecular Systems, Eindhoven University of Technology, 5600 MB Eindhoven, The Netherlands
[e] Department of Marine Technologies, The Leon H. Charney School of Marine Sciences, University of Haifa, Mt. Carmel, Haifa 3498838, Israel
[f] Max-Planck Institute of Colloids and Interfaces, Potsdam-Golm 14476, Germany
[g] Department of Chemical Research Support, Weizmann Institute of Science, Rehovot 7610001, Israel

ARTICLE INFO

ABSTRACT

In reef-building corals, larval settlement and its rapid calcification provides a unique opportunity to study the bio-calcium carbonate formation mechanism involving skeleton morphological changes. Here we investigate the mineral formation of primary polyps, just after settlement, in two species of the pocilloporoid corals: *Stylophora pistillata* (Esper, 1797) and *Pocillopora acuta* (Lamarck, 1816). We show that the initial mineral phase is nascent Mg-Calcite, with rod-like morphology in *P. acuta*, and dumbbell morphology in *S. pistillata*. These structures constitute the first layer of the basal plate which is comparable to Rapid Accretion Deposits (Centers of Calcification, CoC) in adult coral skeleton. We found also that the rod-like/dumbbell Mg-Calcite structures in subsequent growth step will merge into larger aggregates by deposition of aragonite needles. Our results suggest that a biologically controlled mineralization of initial skeletal deposits occurs in three steps: first, vesicles filled with divalent ions are formed intracellularly. These vesicles are then transferred to the calcification site, forming nascent Mg-Calcite rod/pristine dumbbell structures. During the third step, aragonite crystals develop between these structures forming spherulite-like aggregates.

Statement of Significance

Coral settlement and recruitment periods are highly sensitive to environmental conditions. Successful mineralization during these periods is vital and influences the coral's chances of survival. Therefore, understanding the exact mechanism underlying carbonate precipitation is highly important. Here, we used *in vivo* microscopy, spectroscopy and molecular methods to provide new insights into mineral development. We show that the primary polyp's mineral arsenal consists of two types of minerals: Mg-Calcite and aragonite. In addition, we provide new insights into the ion pathway by showing that divalent ions are concentrated in intracellular vesicles and are eventually deposited at the calcification site.

1. Introduction

Biomineralization comprises the formation, structure and properties of inorganic solids deposited in biological systems [1,2]. Scleractinian corals are one of the few calcifying metazoans that produce aragonitic skeletons, and arose in the Triassic period long after the greater proliferation of calcifying corals in the Paleozoic period, which produced calcitic skeletons [3]. Coral calcification is a central biological and geochemical process in the ocean. The tiny polyps of coral colonies build the most important bioconstruction in the world – coral reefs, producing approximately 10^{12} kg of calcium carbonate per year in the form of aragonite [4]. Despite the importance of this process, the exact mechanism underlying the calcium carbonate precipitation is still poorly understood. In the

* Corresponding authors.
E-mail addresses: iddo.pinkas@weizmann.ac.il (I. Pinkas), tmass@univ.haifa.ac.il (T. Mass).

past, two parallel lines of inquiry have emerged; the geochemical model and the biologically controlled model. In geochemical models, nucleation and growth of the calcium carbonate crystals are directly related to seawater carbonate chemistry at thermodynamic equilibrium [5]; the role of the organisms in the precipitation reaction is partly ignored. The biologically controlled model is based on biophysical processes far from the ambient thermodynamic equilibrium. In these processes, ions, proteins and polysaccharides, responsible for the nucleation and growth of calcified structures, are concentrated by the organism in specific compartments creating the optimized conditions for precipitation [6–8]. Currently, there is growing evidence supporting the biological controlled process [i.e., [8–12]], and the ongoing question is focusing on how the animal concentrates and transports the ions from the seawater to the site of calcification. Is it by the transcellular pathways through the cells, with calcium channels [12,13], PMCA (P-type calcium ATPase) [14] or vesicles [10,15]? Or by the paracellular pathways between the cells [16], or possibly it is a combination of the two [9].

Corals have a relatively simple life cycle, involving a short, free swimming larval phase (during which the organism is called planula), and a dominant benthic phase called polyp [17,18]. When the planula settles permanently on a hard substrate, it metamorphoses into a primary polyp, which immediately initiates the formation of a calcium carbonate exoskeleton [19]. Most of the work on coral biomineralization has been performed on adult corals, thus the structure of the mature coral skeleton is well documented [20,21]. Centers of calcification (CoC, called also Rapid Accretion Deposits) are known as to be deposited in fast growing skeletal regions (growing fronts of skeletal structures), whereas other skeletal regions are formed by aragonitic fibers [20,22]. Previous studies on adult coral skeleton have located amorphous calcium carbonate (ACC) [15,23], disordered aragonite phases, poorly crystalline aragonite (pAra) [15,24], and high magnesium content [23,25] in the CoC, whereas in the aragonite fibers, strontium and low amounts of magnesium were detected [25]. The fact that these observations appeared in several coral species may indicate a widespread mechanism in adult coral calcification. Previously we showed that mineral formation starts prior to settlement, during the planktonic stage, where Mg-ACC was detected by SS-NMR analysis, while upon settlement, disordered aragonite was also detected [8]. These observations, however, did not provide spatial information, and therefore offer limited mechanistic detail. Successful mineralization during the early period of settlement is essential and influences the survival capabilities of the coral [8,26]. Therefore, understanding the mechanism underlying $CaCO_3$ crystallization at the early stages of settlement is essential.

Previously Gilis et al. [27] characterized the mineral development of *Pocillopora damicornis* from 12 h to 22 days after settlement. Using Raman spectroscopy of dehydrated samples, they showed that aragonite was the major mineral phase after settlement. The authors also reported that calcite minerals are present during the first day of settlement, characterized by rod-shaped structures and containing high concentrations of magnesium, while the most abundant mineral shapes in a primary polyp were dumbbell-like and semi-spherulite structures [27]. The authors suggested that the source of calcite mineral might be induced by bacteria, especially due to the fact that in adult coral these structures were only observed at lateral tissue extensions, where a thin tissue of corals fragments spreads out and covers the substrate glass slide [16,28–30].

Dumbbell structures were previously observed in two other coral species [16,28–30] as well as in pearl oyster [31]. However, in the pearl oyster the dumbbells are composed of Mg-Calcite, rather than aragonite [31]. *In vitro* precipitation experiments of Mg-calcite (with Ca/Mg molar ratio of four or greater) have shown that the forming crystal displays dumbbell shapes [32–34]. Moreover, as similar mineral structures are induced by some bacteria [35–38] the relationship between dumbbell formation and coral skeletal formation was suggested to result from biologically-induced, carbonate formation processes occurring in the leaky sea-water environment between the organism tissue and the substrate [27].

The aim of this multidisciplinary study is to elucidate the initial development of mineral shapes and phases from the first post-settlement days until the formation of the septa and the filling of the whole basal plate, on the primary polyps of two members of the pocilloporoid stony corals (*Stylophora pistillata* and *Pocillopora acuta*). To study these two dominant and well characterized features of adult skeleton, we combined *in vivo* microscopy and spectroscopy, and molecular biology.

2. Materials and methods

2.1. Planulae collection and settling

Planulae traps were made using a 160 μm plankton net, the top of which was attached to a plastic container. Planulae were collected from adult *S. pistillata* colonies under a special permit from the Israeli Natural Parks Authority, in front of the Interuniversity Institute of Marine Biology (IUI) in Eilat, Israel. Nets were placed on 14 adult corals for several nights during February–May 2016 and 2017, following peak releases [39] (Supplementary Fig. 14). The metamorphosis and settlement processes proceeded naturally in small petri dishes with glass bottoms, which underwent preconditioning treatment with seawater. In addition, *P. acuta* corals were collected on July 2017 (Special Activity Permit 2018-50) from Kaneohe Bay, O'ahu Hawai'i and returned to the Hawai'i Institute of Marine Biology where they were housed in outdoor 1300 L tanks in shaded conditions with an ambient photoperiod and natural diurnal fluctuations in temperature (Supplementary Fig. 14). In order verify the presence/absence of bacteria precipitated minerals in the primary polyp we treated the larva, prior settlement, with 3% antibiotic cocktail (Antibiotic Antimycotic Sigma #A5955), for 3–4 days. We then transferred the larva to filtered artificial sea water for settlement and imaged the primary polyp with light microscopy.

2.2. Polarized Light Microscopy (PLM)

Ten primary polyps of *S. pistillata* were observed and monitored under the light microscope Nikon ECLIPSE TI-E, using a DIC polarized filter. For the time-lapse series, the samples were imaged while they were located in a controlled environment chamber (25 °C & 90% humidity). To determine the growth of skeletal structures (such as dumbbells), DIC images from time-lapse series were processed as follows: Shading (from coral tissue lying above the calcified structures) was reduced by using bandpass filtering in the open-source image processing program Fiji [40]. Contours were then enhanced using the 'Find Edges' command (a 3 × 3 Sobel edge filter). Contours of individual skeletal elements were then traced in the processed images, false-colored and overlaid in Fiji.

2.3. Scanning Electron Microscopy (SEM) + Energy Dispersive X-ray (EDS)

The skeletons of nine primary polyps of *S. pistillata*, three to five days post settlement, and three primary polyps of *P. acuta*, which were three days post settlement, were imaged. The tissue of the

polyp was removed by immersing the dish in 1% sodium hypochlorite (NaClO) for 10 min as described by Gilis et al. [27]. Samples were vacuum coated with carbon (for conductivity) prior to examination under a ZEISS SigmaTM SEM coupled with EDS, by using an in-lens detector (1–1.5 kV, WD = 3.5–5 mm). Elemental analyses by an X-ray Energy Dispersive technique-dispersive X-ray spectroscopy (EDS) were performed in locations of interest that were chosen after imaging in the SEM (10 kV, WD = 5 mm). Elemental distribution maps were obtained using Quantax software.

2.4. RNA extraction, processing and sequencing

Five samples of S. pistillata that included pools of 15 primary polyps, were used for the bacterial population analysis. In addition, triplicates of three developmental stages; planktonic larva, metamorphosed larva and primary polyps were used for the biomineralization tool-kit gene expression pattern. The samples were snap-frozen in liquid nitrogen and stored in 0.55 ml of TRI reagent (Life Technologies) at −80 °C until the RNA extraction. The RNA was extracted using the TRI reagent (Life Technologies) following the manufacturer's protocol with some modification at the homogenization step, as described by Mass et al. [41]. We performed on-column DNase digestion using the PureLink RNA mini kit (Anbion®).

2.5. Bacterial community structure

The RNA used in reverse transcription (RT) reaction, using SuperScript™ (Thermofisher), following the manufacturers protocols. cDNA was used for two-step PCR amplification of partial 16S rRNA. The first PCR reaction was to amplify a region of 16 s with the primers CS1_515F (ACACTGACGACATGGTTCTACAGT GCCAGCMGCCGCGGT) and CS2_806R (TACGGTAGCAGAGACTT GGTCTGGACTACHVGGGTWTCT). The non-underlined sequences CS1 and CS2 tails were amplified in the second PCR reaction with Access Array primers of Illumina from Fluidigm. After the second PCR, the samples were purified using AmpureXP beads (Beckham Coulter) and then checked for concentration by qubit and size by Tapestation. The libraries sequenced on the illumina miseq using a v2-500 cycles kit to generate 2 × 250 paired-end reads. The reads trimmed for adaptors (rCS1 and rCS2 as well as any illumina adaptors), merged and OTU picking performed to generate OTU and Abundance tables, using the CLC-bio workbench software (HyLab, Israel). A total of 79,572 high-quality bacterial sequences from five samples were analyzed. Taxonomic identification was done by alignment to the Silva reference database (version 132), with a cut-off of 80% identity and score of 90.).

2.6. Sequencing, assembly and differential gene expression

RNAseq data were generated using triplicate samples of the three S. pistillata developmental stages. Sequencing libraries were prepared using the Illumina TruSeq kit. An Illumina HiSeq 2500v4 sequencer was used to obtain 60 bp single reads (2 lanes). Poly-A/T stretches and Illumina adapters were trimmed from the reads using cutadapt [42]; resulting reads shorter than 30 bp were discarded. Reads were mapped to 39 genes recently shown to be part of the biomineralization tool-kit in the stony coral S. pistillata [43] using STAR v2.4.2a [44], supplied with gene annotations in gtf format. Expression levels for each gene were quantified using htseq-count [45], using the gtf above. Differential expression analysis was performed using DESeq2 [46], supplied with the design formula ∼ group. Raw P values were adjusted for multiple hypotheses using the Benjamini-Hochberg method.

2.7. Micro-Raman spectroscopy

Sample preparation: eight S. pistillata primary polyps were examined in vivo by Raman, without any pre-treatment. At the end of the experiment, the primary polyps were still alive and continued growing. In addition, two P. acuta primary polyp were fixed in ethanol prior to measurements. Micro-Raman measurements were conducted on a LabRAM HR Evolution instrument (Horiba, France) as described previously by Akiva et al., [8]. The reference spectra used were biogenic aragonite collected from a mature coral and magnesium calcite, which was precipitated and examined as described in Ref. [47].

Raman mapping – Spectra were measured from a rectangular area of each primary polyp and processed as a hyperspectral image using a custom script in Matlab 2018a (Mathworks, Inc.). For each pixel, a window of 30 cm^{-1} Raman shift to the right and left the distinguishing peak of each mineral was isolated (206 cm^{-1} for aragonite, and 284 cm^{-1} for magnesium calcite), and automatically checked if it contained a peak. The criterion for deciding whether or not there was a peak was to see if the maximum value of the signal in that window was at least 20% greater than its mean, and whether the maximum value fell in the middle of the window. If a signal contained a valid peak for both minerals, the one with the larger amplitude was kept. In the resulting map, the distribution of the minerals is visualized in false colors: aragonite in red, and magnesium calcite in green. The intensity of each pixel is scaled by its magnitude in the hyperspectral image.

2.8. XRD/XRF

Six S. pistillata primary polyps from one to four days after settlement were settled spontaneously on kapton foil. For the measurement, the samples were mounted between two aluminium frames, which were attached to the sample holder. The measurement conducted by Wide Angle X-ray scattering (WAXD) and X-ray florescence (XRF) at the mySpot beamline at BESSY II synchrotron radiation facility (HZB, Helmholtz-Zentrum Berlin für Materialien und Energie, Berlin, Germany) [48], using an X-ray spot size of 10 μm and multilayer monochromator (wavelength λ = 0.7293 Å; E = 17 keV). The two-dimensional scattering patterns were recorded using an Eiger 9 detector (3110 × 3269 pixels and 75 μm pixel size). The sample-detector distance was 254.45 mm and the measurement time was 10 s. For calibration, Quartz standard was measured. Data analysis, including calibration, background subtraction and peak fitting were processed with DPDAK software [49]. Peak fit results were used to generate 2D maps, after masking the results based on the intensity of the peak. In addition, 1D maps were plotted for some points of interest in both samples, using Origin software [50]. For XRF measurements we used a fluorescence detector (Bruker XFlash, SDD, window size 10 mm^2) Fluorescences map were generated after calibration, using PyMca software [51].

2.9. Confocal laser scanning microscopy

For localization of calcium particles or evidence of bacteria in the primary polyp living tissue, primary polyps were incubated overnight in 2.6 μM Calcein Blue (Sigma 54375-47-2) dissolved in seawater. Then, they were rinsed for one-hour in seawater before observation. For localization of calcium vesicles, the primary polyps were additionally stained with FM 4-64 (T13320, Life Technologies, OR, USA) membrane dye. Working solution of 5 μg/ml was prepared by diluting the stock solution in artificial seawater. Primary polyps were immersed in the working solution for about 10 min before imaging. For image acquisition of live samples, a Nikon A1 confocal laser-scanning microscope was used with a

plan-apochromatic VC 1.4 N.A. 60× magnifying oil-immersion objective. Images were acquired in four channels, using one-way sequential line scans. Calcein Blue was excited at 405 nm and its' emission collected at 450/50 nm with a suitable PMT gain of 64. Autofluorescence of the coral tissue was excited at 488 nm and its emission collected at 525/50 nm with a PMT gain of 10. Chlorophyll autofluorescence of the symbiotic algae was excited at 488 nm and using a 593 nm long-pass filter at a PMT gain of 101. Differential interference contrast images were acquired using the transmitted light detector at a gain of 38. In all cases, no offset was used, and the scan speed was ¼ frames/s (galvano scanner). The pinhole size was 35.8 μm, approximating 1.2 times the Airy disk size of the 1.4 N.A. objective at 525 nm. Scanner zoom was centred on the optical axis and set to further magnify around 2× to 4×. Axial step size ranged from 0.35 to 1.5 μm, using between 11 and 20 planes per time-point. Time-points were collected every 10 to 15 min.

To quantify colocalisation of particles stained with calcein blue and FM 4-64, we used our previous object-based colocalisation analysis [52]. A summary of the analysis approach can be found in the Supplementary Fig. 13.

2.10. Cryo-scanning electron microscopy (SEM) imaging

Five primary polyps were high-pressure-frozen while they were still alive as described previously by Akiva et al., [8], and were imaged directly in cryo conditions, without coating.

2.11. Immunolocalization

S. pistillata primary polyps were prepared as described previously by Mass et al., [41]. Primary anti-CARPs 1-4 applied at 1:560, 1:35, 1:140 and 1:1400 dilution, respectively, and incubated. Staining specificity was achieved by performing similar control experiments, without the first antibody step.

3. Results

3.1. Crystal morphology

Mineral morphologies in both *S. pistillata* and *P. acuta* were characterized using scanning electron microscopy (SEM) after organic tissue removal (Fig. 1). In the 3 days settled *S. pistillata* primary polyps, the most abundant mineral deposit before basal plate closure are pristine dumbbells (Fig. 1B) and dumbbell-like structures (Fig. 1D, Supplementary Fig. 1) with a size range of ~10–35 μm. Those structures consist of 50–100 nm nanogranular particles (Fig. 1C and E, Supplementary Fig. 1). Dumbbell-like structures grow by the deposition of needle-shaped fibers radiating from the pristine dumbbells (Fig. 1D, F and G). These needles grow in the presence of organic material, seen as fibers in SEM (Fig. 1G).

In contrary, the basic initial mineral morphology observed in 3 days settled *P. acuta* is smaller rod-shaped structures, with a size range of 1–5 μm in length (Fig. 1J, Supplementary Fig. 1K and L). This morphology is different from the pristine dumbbell shapes observed in *S. pistillata* (Fig. 1B). In addition, dumbbell-like minerals that are larger than the rods (15–30 μm) were also observed in *P. acuta* (Fig. 1J, Supplementary Fig. 1). These dumbbells are surrounded by the rod shaped minerals (Fig. 1J blue arrowhead). In both coral species, *S. pistillata* and *P. acuta*, we found that the crystal-structure is similar and is composed of nanogranular particles (Fig. 1C, E and L) from which needle-shaped crystals grow (Fig. 1G and K). These needle shaped crystals consist nanogranules as well (Supplementary Fig. 1F).

The septa and the basal plate are two dominant well characterized features of the primary polyp (Fig. 1A, I). Fig. 1F shows at least five developed dumbbells, with an external layer made of fused needle-shaped crystals, forming the initial septum. The needles point radially from the dumbbells outwards, allowing space filling between two neighbouring dumbbells in order to form the septum structure (Fig. 1F).

In order to track skeletal development and growth, *S. pistillata* primary polyps were imaged *in vivo* using optical contrast microscopy (differential interference contrast (DIC) and polarized light microscopy (PLM)) and long term time-lapse imaging from 1 to 5 days post settlement (Fig. 2). Light microscopy clearly shows that during the first 3 days post settlement the dumbbell-like structures are abundant throughout the periphery, in the forming septum and the basal plate (Fig. 2A–D). *In vivo* PLM shows that the dumbbell-like structures are mostly crystalline (Fig. 2E), and display spherulitic texture, as seen by the characteristic birefringent Maltese-cross pattern in the PLM and DIC images (Fig. 2E–F) [22].

To examine the growth and merging of the dumbbells, time-lapse imaging was acquired using PLM (Fig. 2 G–I, Supplementary Movies 1–2). In movies S1 and S2 we imaged a primary polyp from 1 to 3 days' post settlement. We observed pristine dumbbells merging with larger mineral structures at the edge of the septum in the first 24 h (Supplementary Movie 1). These structures grow and fill the space in a spherulitic pattern. In Supplementary Movie 2 we imaged 48–72 h post settlement, at a different location, in which dumbbells merged with other developed areas of minerals, to form the basal plate.

Dumbbell calcium carbonate structures were suggested previously to be induced by some bacterial species [36,53–57]. We thus examined the possibility of bacterial involvement in the pristine dumbbell formation by comparing larval settlement after bacteria lysis treatment. We did not find any evidence of bacterial clusters in the vicinity of the dumbbells in primary polyp settling in ambient conditions (Supplementary Fig. 3A–B). Moreover, the development of pristine dumbbells and other developed areas of mineral was the same in both treatments (Fig. 2G–I, Supplementary Fig. 3C, Movies 1–3). Additionally, we examined the bacterial community diversity in the primary polyps by 16S rRNA and high-throughput sequencing, finding no evidence of calcium carbonate mineralizing bacteria [35–38] at the genus level (Supplementary Fig. 4 and Supplementary Table 1).

3.2. Elemental composition of the mineral

Elemental composition analysis by EDS, of both coral species reveals that the initial $CaCO_3$ minerals, i.e. the rod-shaped structures in 3 days settled *P. acuta*, and the pristine dumbbell shaped ones in 3 days settled *S. pistillata,* contain magnesium (Fig. 3, Supplementary Fig. 5). However, due to sample topography, quantitative analysis of magnesium concentration cannot be achieved using this setup [58].

The elemental composition analysis also revealed the presence of sulphur and strontium in *S. pistillata* (Fig. 3A, Supplementary Fig. 5). It is possible that the sulfur measured by EDS stems from the remains of the biological matrix surrounding the dumbbells, or the involvement of biomolecules in scaffolding for the building of the needle shaped crystals.

3.3. Crystalline phase

To explore the mineral phases, and the distribution of the magnesium containing minerals in the primary polyps, *in vivo* micro-Raman spectroscopy, X-Ray Diffraction (XRD) and X-Ray Fluorescence (XRF) (on preserved samples) were performed. The *in vivo* micro-Raman spectra of the needle-shaped crystals in both 3 days
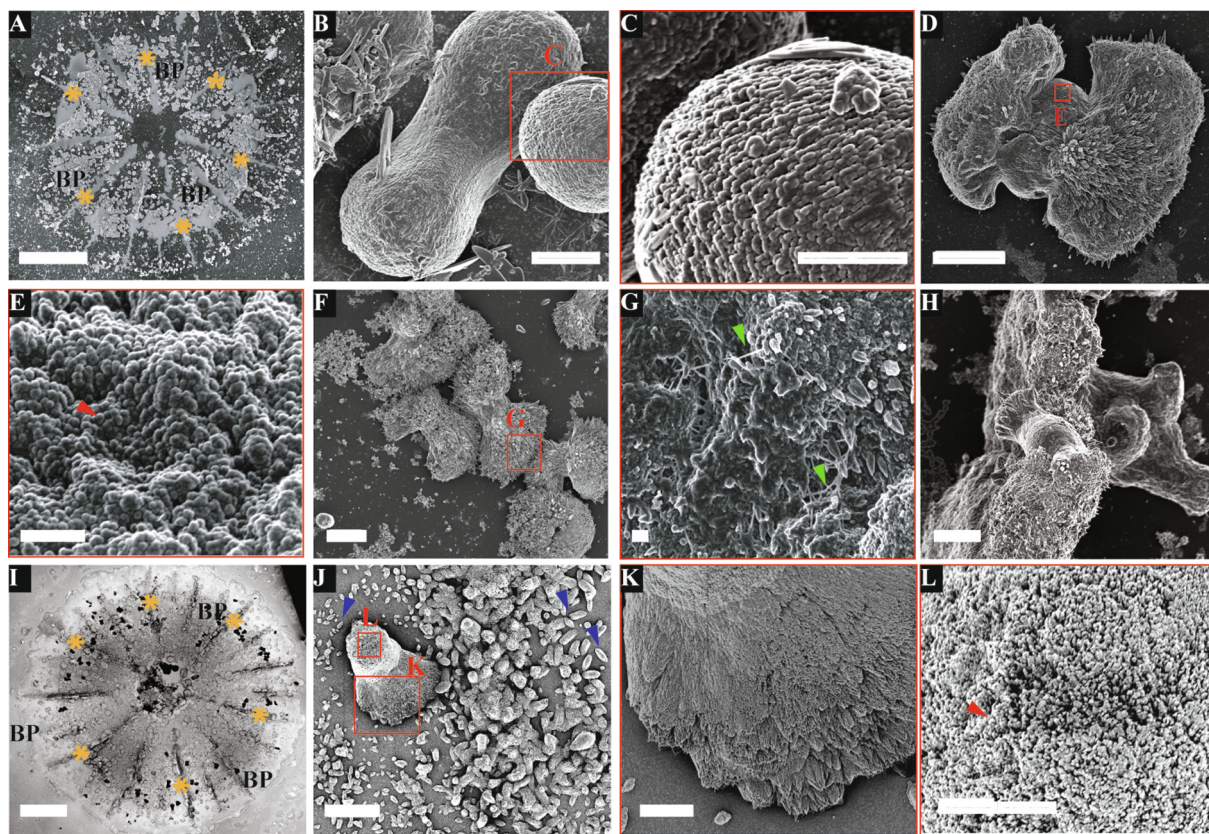
Fig. 1. Early mineral structures in *Stylophora pistillata* and *Pocilopora acuta* primary polyps. SEM micrographs of the mineral deposit structures of 3 days settled *S. pistillata* (A–H) and *P. acuta* (I–L), using an in-lens secondary electron detector. (A, I) Primary polyps of *S. pistillata* and *P. acuta* respectively, after removal of the tissue. (B) *S. pistillata* pristine dumbbells. (C) Higher magnifications of the region depicted in a red box in B showing that the pristine dumbbell is characterized by nano-granules. (D) *S. pistillata* mineral deposition in a developing dumbbell like shape (E) Higher magnification of the region depicted in the red box in (D) The surface structure of the center of the dumbbell showing nano-granules (red Arrowhead). (F) Merged dumbbells connected by needle shaped crystals. The structure is part of a secondary septum. (G) High magnification of the region depicted in the red box in (F), shows that the edges of the dumbbell are composed of needle shaped crystals embedded with organic fibers (green arrowheads) (H) A dumbbell, located on the septum wall elevated from the basal plate plane. (I) *P. acuta* dumbbell basal plate seemingly merging with small rod-shaped structures also forming the septum. (J) *P. acuta* rods (blue arrowheads) and dumbbell-like mineral deposit (K) Needle shaped crystals at the opposite end of the dumbbell. (L) The surface structure of the other end of the dumbbell, made of nano-granular particles (red arrowhead). Orange stars – septa, BP – basal plate. Scale bars: 300 μm (A, I), 2 μm (B, C K, L), 10 μm (D, F, H, J), 500 nm (E, G). (For interpretation of the references to color in this figure legend, the reader is referred to the web version of this article.)

settled *S. pistillata* and *P. acuta*, which grow on top of the developing dumbbells (Fig. 1B, E), are characterized by peaks at 152.4 (B_{1g}), 205 (B_{2g}), 702.6 (B_{3g}), 705.6 (A_g) and 1085.6 (A_g) cm^{-1} (Fig. 4, red). These peaks are characteristic Raman shifts of aragonite [59,60].

The initial growth structures – the small rod shapes in *P. acuta* (Fig. 1J) and pristine dumbbell shapes in *S. pistillata* (Fig. 1B and J), show Raman shifts at 157.5 (E_g), 283.8 (E_g), 714 (E_g) and 1089 (A_{1g}) cm^{-1} (Fig. 4, blue). This set of peaks is similar to those of calcite [60] as well as to dolomite and to magnesite [61] with slight shifts in the wavenumbers of these peaks (see Supplementary Table 2 for full peak assignment). In addition, the linewidth of the above peaks is relatively broad (13.7 (E_g), 20.1 (E_g), 26.4 (E_g) and 10.7 (A_{1g}) cm^{-1}) when compared to the more crystalline aragonite peaks (11.4 (B_{1g}), 9.9 (B_{2g}), 3.7 (B_{3g}), 4.4 (A_g) and 4.3 (A_g) cm^{-1}). Fig. 4A also shows a line scan between the developed dumbbell in the forming septum and the pristine dumbbell structure in *S. pistillata*, similar to the structures observed in Fig. 1B. The spectral profiles in the scanned line in Fig. 4B shows that there is a clear shift in spectral features from Mg-calcite found in the pristine dumbbell (Fig. 4B spectra 9–10) to aragonite at the forming septum (Fig. 4B spectra 1–6). This is most clearly seen in the A_g/A_{1g} peaks in Fig. 4E. Supplementary Table 3 lists the Raman line width for each/several scattering peaks.

Micro-focused Scanning XRD coupled with XRF measurements were performed on *S. pistillata* primary polyps at different times post settlement. The XRD patterns obtained from each measured volume with lateral beam cross-section of 10 × 10 μm^2 show typical reflections of either aragonite, Mg-calcite or mixtures of both. In the q range probed in this experiment are the (0 1 2) and the (1 0 4) reflections of calcite that are used as markers for Mg-calcite. Here q (0 1 2) = 16.3 ± 0.04 nm^{-1} and q (1 0 4) = 20.76 ± 0.03 nm^{-1}. Thus the peak positions of the Mg-calcite reflections are shifted with respect to pure calcite (where q (0 1 2) = 15.5 nm^{-1} and q (1 0 4) = 20.5 nm^{-1}) [62]. The fact that the contribution of magnesium, incorporated into the calcitic crystalline lattice, causes peak shifts to higher wavenumbers is well documented [62]. This effect is much larger than the contribution of organic induced lattice distortions [63]. Similar peak shifts are seen in the XRD profile of *Paracentrotus lividus* sea urchin spine powder (Supplementary Fig. 7) where 3% Mg^{2+} concentration was determined by quantitative elemental analysis [64], suggesting similar Mg^{2+} concentration in sea urchin *Paracentrotus lividus* spines and *S. pistillata* primary polyps.

Pure aragonite is characterized by peaks at q (1 1 1) = 18.5 nm^{-1}, q (0 2 1) = 19.5 nm^{-1} and q (0 1 2) = 23.3 nm^{-1} [65]. In our measurements, all these peaks were slightly shifted to lower peak positions (Fig. 5, Figs. S7–S9), probably due to the incorporation of strontium into the lattice. However, unlike Mg-calcite, which largely displayed no variation in peak-position across the different samples, here we observe relatively large variations likely
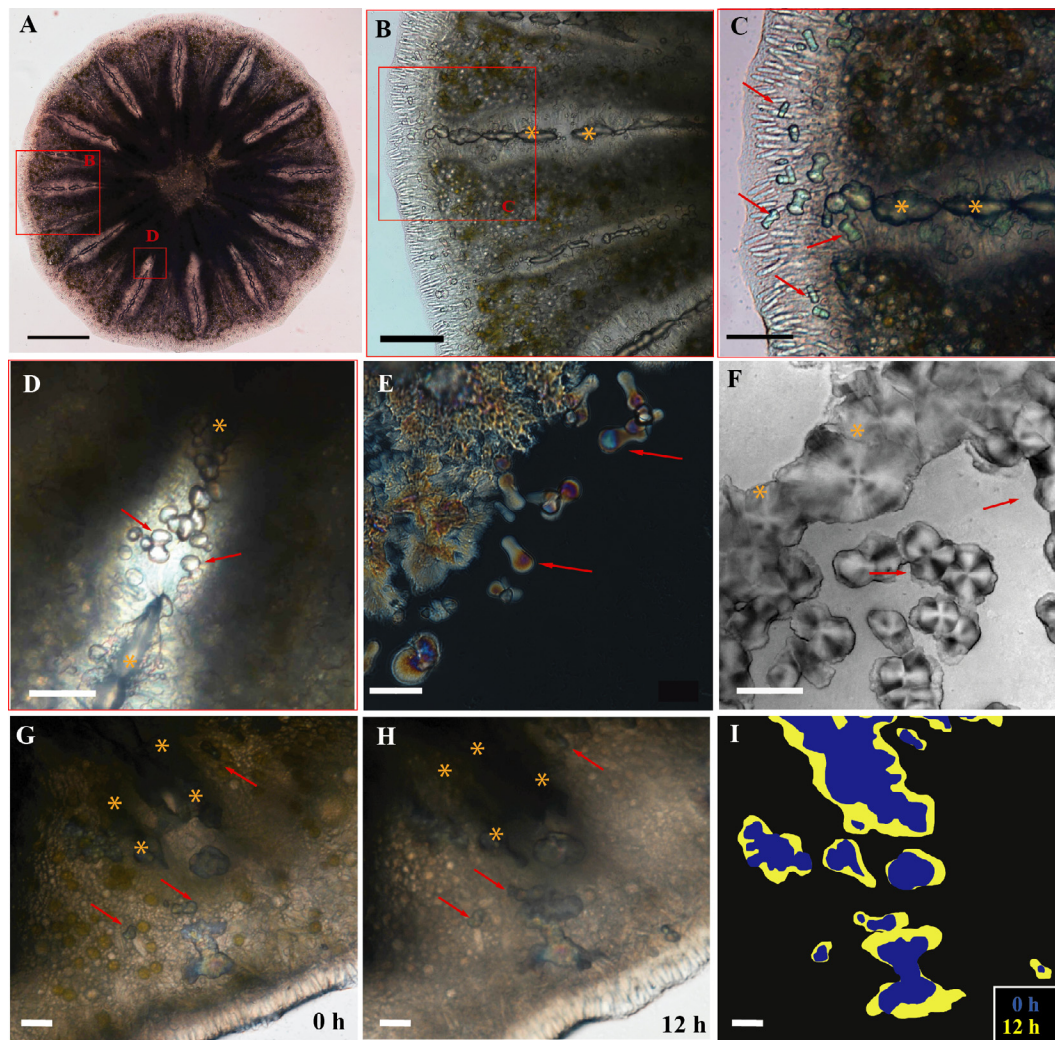
Fig. 2. Dumbbells grow by a spherulitic growth pattern, and then merge to form the septa and basal plate in 3 days settled *S. pistillata* primary polyps. (A–D) *In-vivo* Light Microscopy images (A) *S. pistillata* whole primary polyp. (B–D) Higher magnifications of the regions marked by the red boxes in A and B showing the developing septa (Orange asterisk) and the high abundance of pristine dumbbell structures (red arrows) (B), pristine dumbbells in the periphery and ones that are forming the basal plate and septum (see also C and D). (E) cross-polarization image of pristine dumbbells and the basal plate (F) DIC image of *in-vivo* confocal microscopy of the lower level (z-stack) of the septum and basal plate showing the Maltese crosses typical of birefringence with spherical symmetry [1] (i.e. the crystal structure has a radial arrangement) (G–I) Time points of 14 h time-series of primary polyp, 1 day post settlement (see the full movie in Supplementary 1 and 2). (G) The first time point (H) 12 h after the first image (I) Overlay of false-color images of (G, blue) and (H, yellow). Orange asterisks – septa, red arrows – pristine dumbbells. Scale bars: 250 μm (A), 50 μm (B) 20 μm (C–I). (For interpretation of the references to color in this figure legend, the reader is referred to the web version of this article.)

resulting from variable Sr^{2+} content. For example, in samples fixed after 1 day of settlement sample q (1 1 1) = 18.53 ± 0.05 nm^{-1}, whereas in the 2–4 days settled samples, the peak position shifted to 18.31 ± 0.04 nm^{-1}, indicating higher Sr content in the mature mineral particles.

Fig. 5 shows elemental and mineral phase distribution obtained from polyps one day post settlement. Here we find small aggregates of mineral particles in a size range of 20–50 μm, composed of either Mg-calcite or aragonite as indicated by scanning-XRD measurements (Fig. 5C–F), which show typical XRD profiles of the two mineral phases (Supplementary Fig. 8). The elemental distribution map shows overlapping distribution of calcium (Fig. 5B blue pixels) with both Mg-calcite and aragonite particles, and co-localization of Sr^{2+} and Ca^{2+} (Fig. 5B. magenta pixels) in regions assigned to aragonite. Sr^{2+} is absent from regions assigned to Mg-calcite (we note that in our experimental set-up Mg^{2+} XRF cannot be detected).

We have not been able to detect Mg-ACC or ACC as precursors to Mg-calcite or aragonite in our experimental set up. However due to the low sample volume we cannot rule out their presence in small amounts or as unstable precursors.

Next, we mapped 450 × 100 μm^2 region of a growing septum of a primary polyp two days post settlement. Here, aragonite was the most abundant crystalline form (Fig. 6B), forming the growing septum and the surrounding basal plate. Mg-calcite was detected in small regions along the developing septum together with aragonite (Fig. 6C. lines 3–8). We note that as the aragonite intensities are much higher in these areas (Supplementary Fig. 9) and due to the sampling step size (10 μm), Mg-calcite mineral particles may be partly overlooked. Our oldest sample (four days post settlement) shows a similar trend to the 2 days post settlement sample, where aragonite is the most abundant phase and small regions of both aragonite and Mg-calcite crystals co-exist (Supplementary Fig. 10).

In some of the sampling points, the minor peaks were not detected (i.e. 16.3 nm^{-1} in Mg-calcite, and 23 nm^{-1} in aragonite), due to either different crystal orientation or low relative intensity. The intensity, peak position and the peak width of all five reflec-
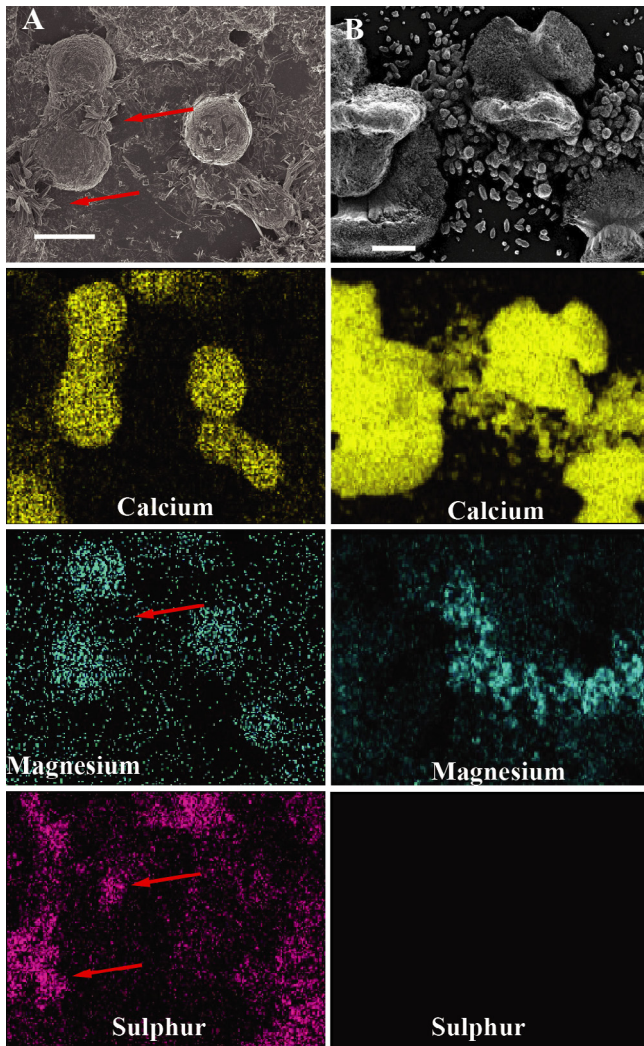
Fig. 3. Elemental distribution in different mineral structures in 3 days settled primary polyp. (A–B) Energy Dispersive X-ray Spectroscopy (EDS) maps of pristine dumbbells from *S. pistillata* (A) and the developing septum from *P. acuta* (B). Each panel contains an SEM image of the areas sampled by the EDS, and the distribution maps for each of the detected elements. In *S. pistillata* (A) calcium, magnesium and sulphur are observed. The pristine dumbbells centers are rich in magnesium, and in some developed areas (showing needle shaped fibers, red arrow) there is high concentration of sulphur, which may point to the surrounding biological matrix or the involvement of biomolecules in the scaffolding for the growing crystals. In *P. acuta* (B) calcium and magnesium were detected but not, sulphur. In this species, the small micron size rod shaped structures that surround the dumbbell-like structure are magnesium rich. Scale bars: 10 μm (A–B).

tions ((0 1 2), (1 0 4) for Mg-calcite and (1 1 1), (0 2 1) and (0 1 2) for aragonite) in the measured q-range are mapped in the Supplementary Figs. 8–10. The parameter maps yielded similar trends for all the reflections.

3.4. Biomineralization "tool-kit" genes

To examine the biological involvement in the mineral formation, we assessed the temporal and spatial expression pattern of putative biomineralization related genes [43] of *S. pistillata* after settlement.

Thirty-seven genes, previously described as components of the biomineralization 'toolkit' (Supplementary Fig. 11), encoding proteins containing one or more trans-membrane domains, extracel-

lular matrix proteins and coral acid-rich proteins (CARPs) were differentially expressed. Thirty-two of those, including CARPs 1, 3 and 4 were upregulated upon settlement, while CARP 2 was down-regulated in this stage (Supplementary Fig. 11A). Immuno-histochemical (IHC) analysis of those CARPs revealed that CARPs 1, 3 and 4 were abundant in the calicoblastic layer around the septa, whereas CARP 2 was abundant at the base of the mesentery (the base of the tentacles) (Supplementary Fig. 11B–E).

3.5. Ion rich vesicle distribution

To examine the formation of dumbbells, we used fluorescence microscopy on nine *S. pistillata* primary polyps stained with calcein blue and FM 4-64 (Fig. 7A–C). Calcein binds divalent alkaline earth metal ions such as Ca^{2+} and Mg^{2+} and is a water-soluble molecule that cannot penetrate the cell membrane by diffusion or through ion channels. Therefore, calcein is used as an indicator of the pathway which calcium is delivered to the skeleton. Calcein-incubated samples show the presence of divalent metal ions in the coral tissue within and outside of cells, as well as in the extracellular matrix and skeleton (Fig. 7Ai). In two days settled primary polyp, two different structures were labelled with calcein blue: punctate structures of small size (0.54 ± 0.15 μm; Fig. 7Ai, magenta arrowheads) and far larger dumbbells (sizes above 3 μm; Fig. 7Ai, cyan arrowheads).

Calcein blue staining showed no cytotoxic effects and was still visible in a growing primary polyp 14 days after labeling (Supplementary Fig. 12A). In addition, control primary polyp samples that have not been incubated with calcein blue, show only the fluorescence in the green region (488/509 nm Excitation/Emission) due to the presence of intrinsic green fluorescence proteins (GFP) (Supplementary Fig. 12B).

The lipophilic dye FM4-64 was used to stain phospholipid membranes, revealing individual cell borders as well as small, isotropic, membrane-enveloped structures (Fig. 7Aii). Some of these membranous particles (10–30%) co-localize with the small calcein-stained particles (Supplementary Fig. 13), suggesting that ion-rich, calcein-stained material is enveloped by phospholipid membranes (Fig. 7B). These small membranous structures, likely vesicles, are distinct from the calcein-stained dumbbell structures in size and location: They are located within FM 4-64 demarcated cell boundaries, while the pristine dumbbells form the exoskeleton septum and the basal plate. The difference in location is also visible in orthogonal sections (Fig. 7C), where round dumbbell is adjacent to the glass surface of the microscope slide, while the putative vesicles are found higher up (away from the glass slide) in the coral tissue. Furthermore, by using Cryo-SEM on freeze-fractured + primary polyp, we observed vesicles that contain highly dense material, as determined by using the backscattered electron detector (BSE), with a uniform size distribution (2–3 μm) inside cells (Fig. 7Di–iii).

Next, confocal microscopy was performed with double staining; Calcein blue indicating divalent ions, and the lipophilic dye FM 4–64 which stains plasma membranes. Calcein stained the exoskeleton mineral dumbbells that form the septum and the basal plate (Fig. 7Ai–Aiv). It can be clearly seen that there is a separation of the tissue from the mineral structures.

The FM4-64 stain shows the cell separation according to the boundary membrane (Fig. 7Aii, Bii). In addition, membrane-surrounded organelles were detected (Fig. 7Bii). Interestingly, 10–30% of these organelles are co-localized with small particles (0.54 ± 0.15 μm) positively stained with Calcein (Fig. 7Biii). The average co-localization distance between the intracellular compartments and the small calcium particles is 0.28 ± 0.12 μm (Supplementary Fig. 13), suggesting that these particles may be extracellular vesicles.
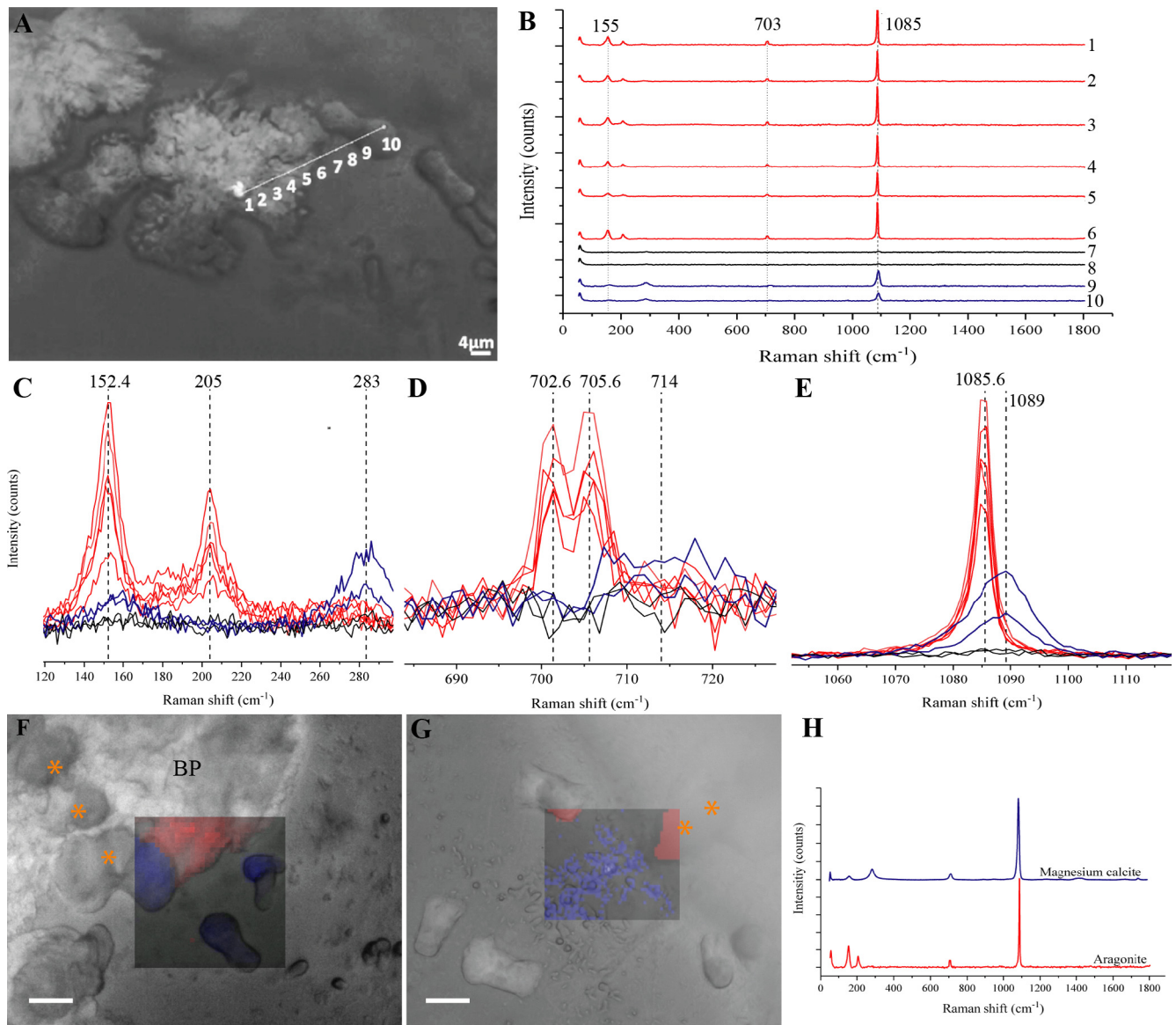
Fig. 4. Raman measurements Mg-calcite and aragonite minerals in early mineral formations – (A) a light microscopy image of a forming septum. In this area, a line scan is drawn between a forming CoC (1) and a pristine dumbbell (10) in 2 days settled *S. pistillata*. The line scan was measured by *in vivo*-Raman spectroscopy (B), the numbers of the spectra correspond to the positions numbered on the cross section. The mature dumbbell shows the spectrum of aragonite (spectra 1–6) and the pristine dumbbell has the spectrum of Mg-calcite (spectra 9–10). The aragonite peaks can be associated with specific symmetry groups of their respective irreducible representations (C–E) following the analysis of De La Pierre et al. [60]. The Mg-Calcite specific peaks are characterized by a shift [61] from the known calcite peaks [60] 283 cm^{-1} line instead of 281 cm^{-1} C), the 714 cm^{-1} line instead of 712 cm^{-1} (D) and 1089 cm^{-1} instead of 1086 cm^{-1} (E), (F–G) Raman spectroscopy maps obtained at the periphery of 3 days settled primary polyps of *S. pistillata* (F) and *P. acuta* (G). There are two crystal forms in these Raman maps; Mg-calcite (blue) in the pristine dumbbells, at the edge of the forming septum (orange asterisk) in *S. pistillata* and the rod-shaped structures in *P. acuta*; and aragonite (red) in the basal plate (BP) and septum in *S. pistillata* and *P. acuta*, respectively. (H) Standard spectra of synthetic Mg-calcite (blue), precipitated as described in Gabriel et al. [47] and of geological aragonite (red). The maps (F–G) were generated according to these spectra using Matlab. Scale bars: 4 μm (A), 10 μm (F–G).

The Calcein stained vesicles are distinct from the dumbbell structures in size and location; the vesicles are much smaller (0.54 ± 0.15 μm) whereas the minimum mineral deposition structures have a diameter of 3 μm. In addition, the vesicles are located within the tissue while the pristine dumbbells form the exoskeleton septum and the basal plate (Fig. 7A). Furthermore, using Cryo-SEM on freeze-fractured settled larvae, we observed vesicles containing highly dense material as determined using the backscattered electron detector (BSE), with a uniform size distribution (2–3 μm) inside cells (Fig. 7Di–iii).

4. Discussion

The settlement and recruitment periods in the coral's life cycle are considered to be highly sensitive to environmental conditions [17,18]. Successful mineralization during these stages increases the chance of survival by growing and developing the skeleton while attached to the substrate [8,19]. Therefore, understanding the mechanism underlying carbonate precipitation is crucial. In the primary polyp, as there is only a small amount of mature skeleton during this stage, it is easier to observe the skeletogenesis
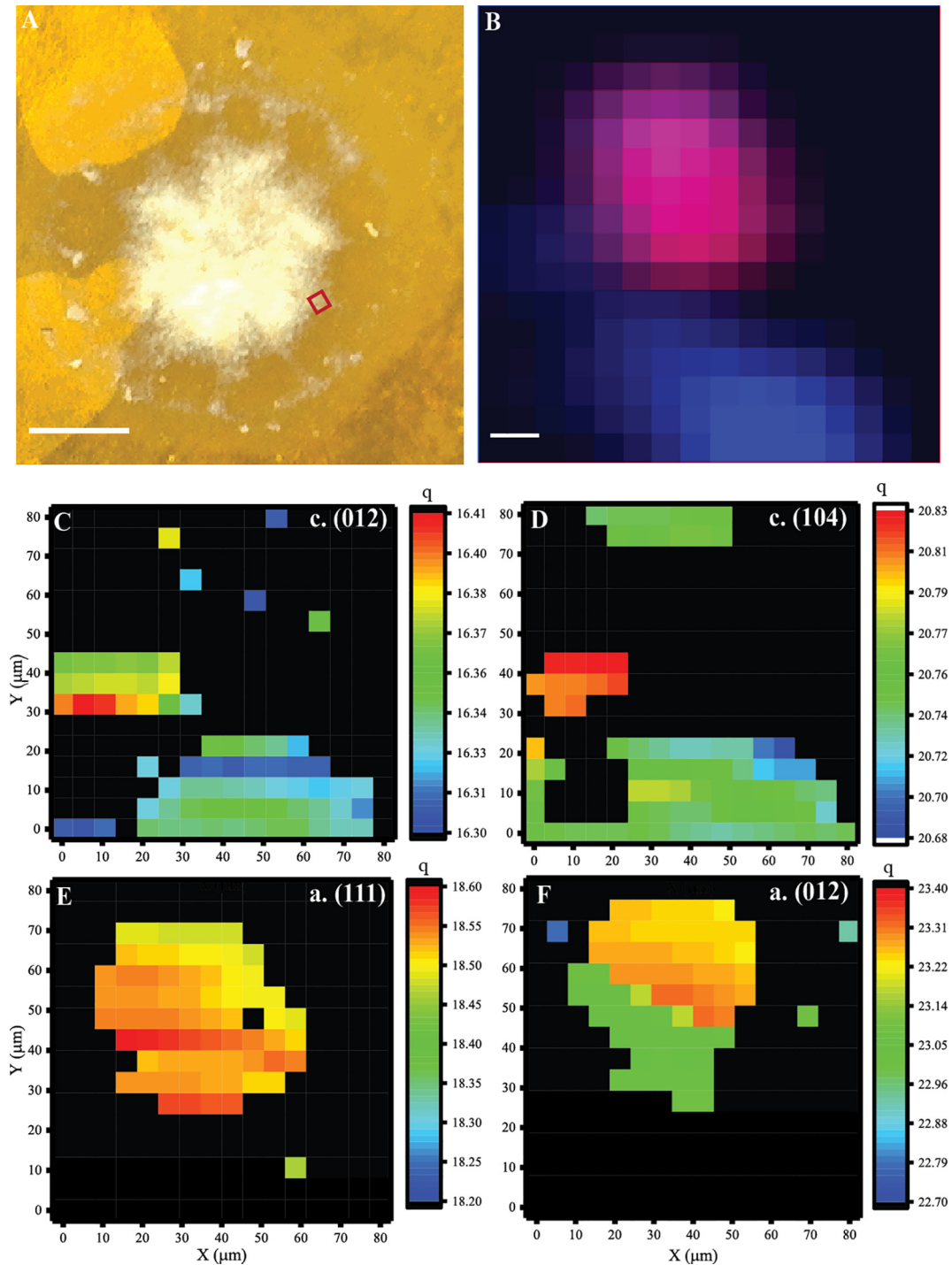
Fig. 5. XRD and XRF maps of the mineral formed during the first day of settlement in *S. pistillata* – (A) Light microscopy of the 1 day settled *S. pistillata* primary polyp (B) 80 × 80 μm XRF map of the region depicted in the red box in (A). Calcium is displayed in the blue channel, strontium in the red channel (arbitrary units) Co-localization of Sr^{2+} and Ca^{2+} appear as magenta (C–F) corresponding XRD maps of the same region as B: peak position maps of specific reflections characterizing Mg-calcite: (C) (0 1 2)-reflection, (D) (1 0 4)-reflection and aragonite (E) (1 1 1)-reflection and (F) (0 1 2)-reflection. The color scale indicates the peak position q (nm^{-1}). Fig. 7 show the peak position, intensity and width of all the examined reflections. Scale bar: A-450 μm, B-20 μm.

process. One of our major observations is that there are several mineral phases correlated with different skeletal structures in the primary polyps. We suggest that biological involvement determines the mineral phase and crystal structure by specific proteins and/or by controlling the magnesium/strontium supply to the calcifying fluid and to the vesicles. It has been previously suggested that Mg^{2+} and Sr^{2+} ions are incorporated into the different mineral crystallites in adult coral by disparate pathways [8,25].

Our observation indicates that the initial mineral structures is varied in *S. pistillata* and *P. acuta* (Fig. 1). This species-specific morphological variation suggests at least some level of biological control. Furthermore, the crystal-structure in both species is
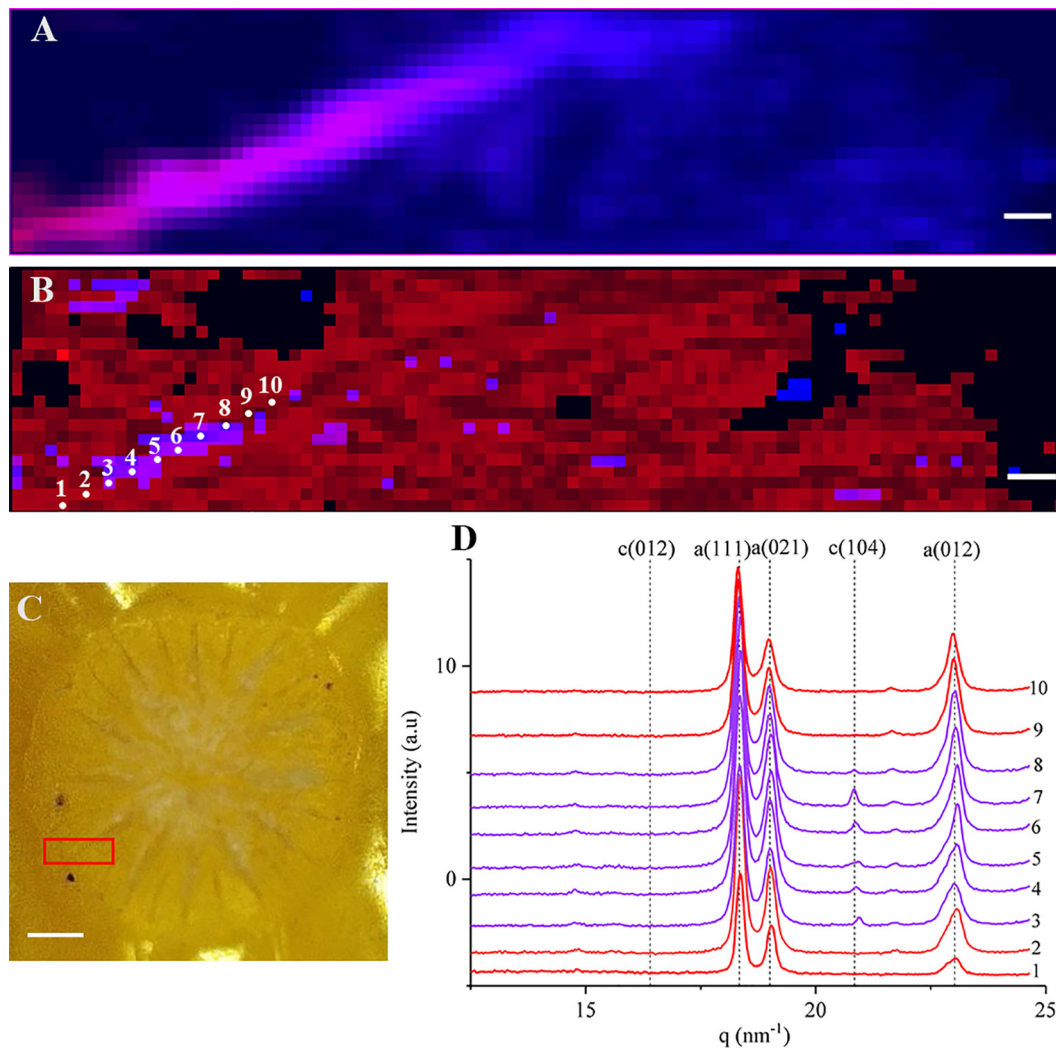
Fig. 6. Scanning XRD and XRF of the forming septum of a two days post-settlement *S. pistillata* primary polyp. (C) Light microscopy image of the two days post-settlement primary polyp. The region depicted in the red box represents the $450 \times 100\ \mu m^2$ area of a developing septum. (A) XRF map of the elemental composition, in which calcium is displayed in the blue channel and strontium in the red channel, co-localization of Sr^{2+} and Ca^{2+} appear as magenta. (B) XRD map of the mineral phase distribution. Mg-calcite (blue) color scale is based on the reflection of calcite (c(1 0 4)) and position after masking the noise based on the intensity. The aragonite (red) color scale is based on the peak position after masking the noise based on the intensity a(1 1 1)-reflection (Supplementary Fig. 9 shows the peak position and intensity 2D maps). (D) XRD profiles of the cross section in (B). The numbers of the profiles correspond to the positions numbered in (B). The forming septum shows typical aragonite XRD profiles (1–2, 9–10, in red) as well as XRD profiles of a mixture of Mg-calcite and aragonite phases (3–8, in purple). Scale bar: A,B – 40 μm, C − 200 μm.

composed of nanogranular particles. These rods and dumbbells serve as a foundation for the growth of aragonite needle shaped fibers radiating outwards, forming the septum and basal plate (Figs. 1–2; Supplementary Movies 1–2). The needle structures also show nano-granular particles, which are embedded within organic material (Fig. 1G). These morphologies are similar to the ones observed by Gilis et al. in *P. damicornis* primary polyps [27].

The pristine dumbbells are highly abundant in the first few days post settlement (Figs. 1–2). However, in adult corals dumbbells were observed only at the lateral growing edge [16,28–30]. We suggest that the dumbbells appear as the earliest calcification structures at any location on the basal plate and on the septum (as illustrated in Fig. 1H), forming a new CoC, and next are overgrown by aragonite fibers formed during next growth phase [23]. Thus, the dumbbells are no longer seen in the adult skeleton. Gladfelter 1983 [66], observed similar growth pattern in *Acropora cervicornis* across the diel cycle. She showed that during nighttime, randomly-oriented fusiform-shaped crystals are forming, and during the day these crystals were hidden by the rapid growth of needlelike crystals. Nanogranules as well as needle-shaped fibers are found in various adult coral species' skeletons [23,20]. In adult corals, the nanogranular clusters are referred to as the CoC or early mineralization zones [20], while the needle-shaped fibers that emerge from these CoCs are referred as the Rapid Accretion Deposits or Thickening Deposits [20].

We identified the pristine dumbbell and the rod-shaped structures as nascent Mg-calcite (Figs. 4–6), while the needle shaped fibers are identified as mature aragonite. Our observation of these two mineral phases is supported by two distinct methods (*In vivo* micro-Raman spectroscopy and XRD, Figs. 4–6). Previous studies have shown traces of calcite [67,68] and low Mg-calcite [69] in CoC of adult corals, and in larval skeleton [70,71] of few coral species. These calcite units have been suggested to originate from endolithic algae [68] or to form by induce mineralization bacteria [27,70]. Our results indicate that there is no evidence of bacteria around the dumbbells nor of mineralization inducing bacteria in the primary polyps (Supplementary Fig. 4 and Supplementary Table 1). *In vivo* PLM images reveal that pristine dumbbells are
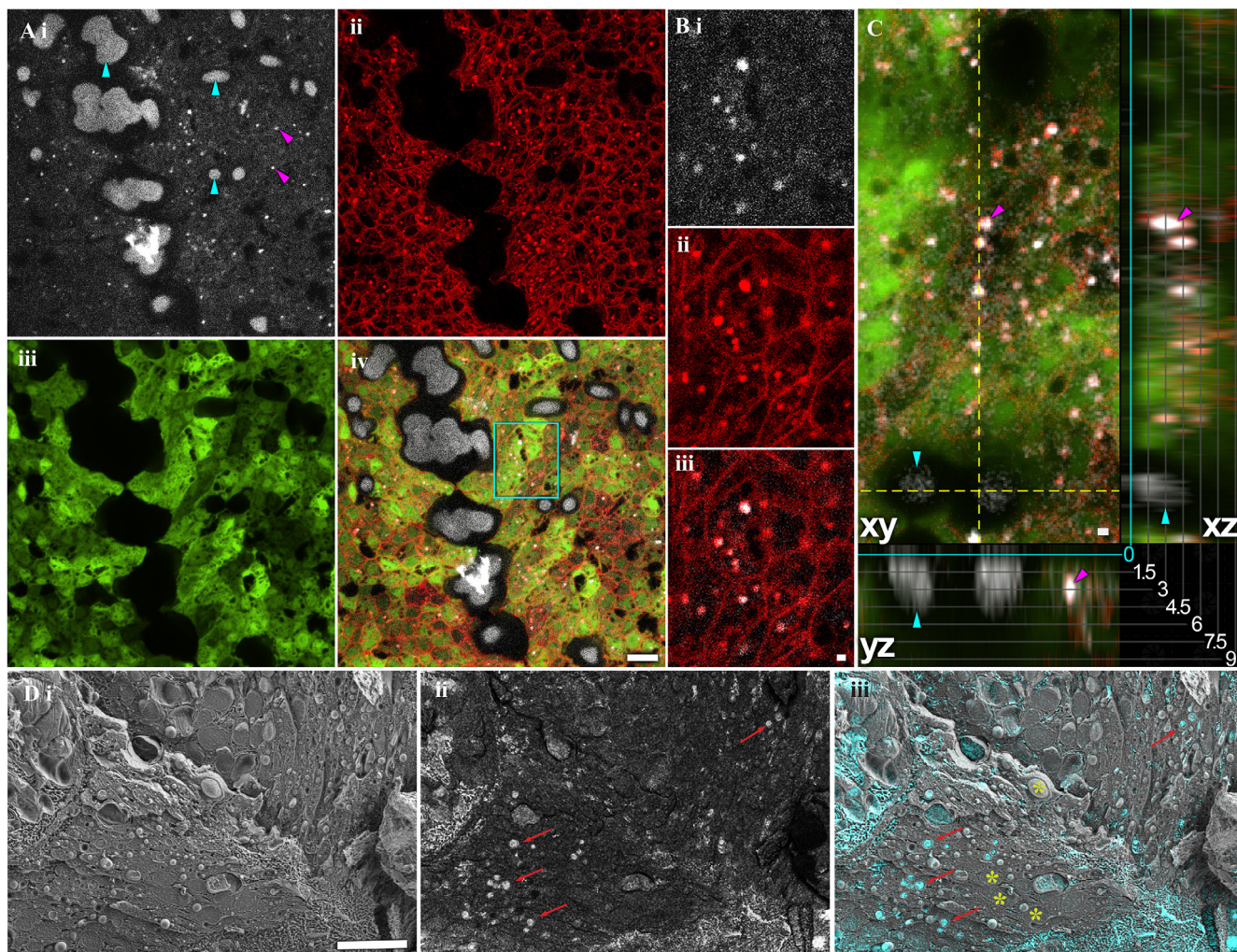
Fig. 7. Vesicle distribution in a calcifying *S. pistillata* primary polyp and planula – (A) *in vivo* fluorescence confocal microscopy of 2 days settled primary polyp. A i) Calcein blue fluorescence signal, displayed in white. Calcified skeletal elements (including mature dumbbell-shaped structures) are indicated by cyan arrowheads. Small vesicles are indicated by magenta arrowheads. The septum, running from top left to down middle, is composed of dumbbell-like structures. ii) FM 4-64 membrane fluorescence marker (red), showing individual cell borders and intracellular compartments. iii) Autofluorescence of the coral tissue layer, containing native green fluorescent protein (GFP). iv) Overlay of i–iii. (B) Higher magnification of the region depicted in the cyan box in (Aiv). B i) Calcein Blue staining. ii) FM 4-64 membrane marker staining. iii) Overlay of i–ii showing partial colocalisation of calcein blue and membrane marker. (C) Orthogonal view (xy/xz/yz) of three-channel overlay (Calcein Blue, FM 4-64 and tissue autofluorescence). The cutting axes for the orthogonal sections are indicated by dashed yellow lines. The numbers (μm) and corresponding grey lines indicate the distance from the glass slide (0, cyan line) to reveal that calcified skeletal elements (cyan arrowheads) touch the glass slide, while vesicles (magenta arrowheads) are above it and hence likely intracellular. (D) Freeze-fracture Cryo-SEM micrograph of *S. pistillata* primary polyp i) SE mode: part of the planula where small uniform 2–3 μm intracellular vesicles are visible (red arrows) with strong backscattered electron (BSE) signal (ii): iii) BSE image (cyan) overlaid on the SE micrograph. Yellow asterisk – nuclei. Scale bar; A – 10 μm; B, C – 1 μm; D – 10 μm.

largely crystalline (Fig. 2E). Larger dumbbells are characterized by the appearance of Maltese Crosses (Fig. 2F) indicative of spherulitic growth pattern [22]. This growth pattern [22] has been demonstrated in adult coral's CoC [72,73] and is associated with a high growth rate [74] and efficient space filling [72].

Nevertheless, the broad Raman spectral linewidth (Supplementary Tables 2–3) suggests that Mg-calcite is poorly crystalline or disordered crystallites. Although nanogranular structures have been suggested to characterize the morphology of ACC in many other carbonate biominerals [75,76], we have not been able to detect Mg-ACC nor ACC as precursors using Raman or XRD in *S. pistillata* and *P. acuta*. However, the possibility that ACC exists in small amounts or as a transient phase cannot be ruled out, especially since long range order which contributes to the Raman cross section does not exist in the amorphous precursors and the XRD measurements were performed on fixed samples. For example, sea urchin larval spicules, are birefringent in PLM despite being largely composed of ACC [77]. This effect was attributed to the coexis-

tences of small particles of ACC and calcite in close proximity at length scales of tens of nm [78].

Based on the XRD results, Mg^{2+} is incorporated into the Mg-calcite phase presence in the CoCs. We estimated the concentration of Mg^{2+} in the pristine dumbbells (based on the peak shift of the XRD profiles (Supplementary Fig. 7), to be around 3%. Strontium was detected mostly in the septa and basal plate where well-developed aragonite crystals are observed (Figs. 5, 6, Supplementary Fig. 9). Based on the XRD aragonite peak shift [79,80] we estimate the concentration of Sr^{2+} incorporated into the aragonitic crystalline lattice positions, to be at maximum of 1 mol %. These result are in line with nanoSIMS measurements on coral skeleton [25].

Fluorescence confocal microscopy and cryoSEM (Fig. 7) reveal small intracellular membrane surrounded dense bodies that contain either Ca^{2+}, Sr^{2+} or Mg^{2+} ions (or mixtures of those). Recent in-vivo study has shown that Ca^{2+} concentration is increasing at the calcifying fluid compared to seawater [12]. The authors

suggested that the ion pathway to the site of calcification is involved with the transcellular pathway through the cells [12]. In order to maintain a high concentration of calcium in the cells, Ca^{2+} must either be bound to Ca^{2+} binding proteins or sequestered in vesicles [25]. Vesicles were observed previously in corals [7,81,82], however their origin and content were not clear. Recently, a Na^+/Ca^{2+} exchanger was identified in *Acropora yongei* and cloned. The authors showed that it contained a peptide signal, which targets proteins to vesicles from the secretory pathway [10]. In addition, intracellular mineral particles containing a mixture of ACC, H_2O-ACC and pAra were observed in adult corals, and have been suggested to be contained in vesicles [15]. Ohno et al., [29] observed similar particles and characterized them as floating putative nascent crystals. The authors observed these particles in a time-lapse sequence, and noticed that over time these particles would appear, and then be relocated to other areas in the cells. It is conceivable that these vesicles contain precursor minerals such as ACC or Mg-ACC.

The identification of a Mg-calcite phase is in agreement with *in vitro* precipitation experiments performed in the presence of CARP3, derived from the coral *S. pistillata* and putatively associated with the mineralization process [47], demonstrated the formation of Mg-calcite. The authors suggested that CARP3 can shift the kinetics of $CaCO_3$ crystallization in seawater-like solutions to Mg-Calcite, instead of aragonite which precipitates in the absence of CARP3. A similar experiment performed with an acidic protein (PfN44) derived from the pearl oyster, showed that it plays a role in regulating the magnesium content of crystalline carbonate polymorphs, stabilizing Mg-calcite and inhibiting aragonite deposition [31].

We examined the temporal and spatial expression pattern of biomineralization "toolkit" genes [43]. The expression pattern showed up-regulation of most of these genes after settlement. A similar trend was observed recently in *Pocillopora darmiconis* [41], *Acropora millepora* and *Acropora digitifera* [83]. The facts that most of the CARPs were highly expressed after settlement, and mostly localized in the calicoblastic cells next to the mineral support their specific role in the biomineralization process. One exception is CARP2 which is down-regulated after settlement and localized in the mesentery (the base of the tentacles). A recent study correlated CARP2 with the ACC phase in the pre-settled planula, in which the authors suggest that this gene is associated with the formation of mineral precursors [8]. CARP2 was identified in adult corals and was associated with the more soluble region of the growth layer in the skeleton [11]. The authors suggested that CARP2 has a role in the skeleton extension during the night [11].

Thus, the observation of biomineralization specific proteins expressed in temporal and spatial relationship to skeletal formation, indicates some degree of biological control over mineral precipitation. The exact role of each gene however remains an enigma.

The presence of co-existing Mg-calcite and aragonite crystallites in 2 and 4 day old samples (as determined by XRD) rules out the possibility of dissolution of the entire Mg-calcite particles and recrystallization of aragonite instead (Fig. 6, Supplementary Figs. 9 and 10). Clearly, the material in the CoCs is not a precursor for aragonite formation, but it may serve as a surface for aragonite needles to grow on. An *in vitro* precipitation experiment demonstrated that aragonite can be precipitated directly on top of calcite, without any organic additives, by adding Mg^{2+} ions to the precipitating solution [84]. Thus, it is conceivable that the organism controls the precipitating environment to favor either Mg-calcite or aragonite at different times/locations. Furthermore, Mg-ACC has been recently identified in the pre-settled *S. pistillata* larvae [8], while in adult coral ACC and pAra were previously observed [15,23]. In this study however, we cannot determine unequivocally whether one or two precursor phases (for aragonite and for Mg-calcite) exist, or that the same precursor transforms to Mg-calcite or to aragonite depending on the Mg^{2+}/Sr^{2+} concentration in the calcifying fluid, and/or the presence of specific biomacromolecules such as CARPs [47,8,85] or others [86]. However, based on previous reports [15,23], it is most likely that Mg-calcite and aragonite are formed from variable ACC precursors. Isotopic labeling experiments [25] have demonstrated that Sr^{2+} and Ca^{2+} are delivered to the mineralizing site through the same voltage-sensitive, transcellular pathway located at the calicoblastic ectoderm, while magnesium is delivered to the surface of the growing skeleton by a different and more actively controlled mechanism. Magnesium can either be actively pumped through the calicoblastic ectoderm to the mineralizing surface, or be introduced by allowing sea-water to enter the mineralizing zone directly [25].

Sulphur on the other hand, shows a complimentary trend to the Mg^{2+} ions one. Organic sulphur was detected previously in three coral species [87,88]. The authors suggested that the high count of sulphated polysaccharides in the developed mineral play a role in the mineral crystallization either by increasing the acidic nature of the skeletal organic matrix (SOM), binding calcium ions, or by altering the local anionic environment, resulting in concentrating the calcium ions at the nucleation points [86–89]. Sulphur may also indicate the presence of proteins, which can also be used as scaffolding for crystal formation.
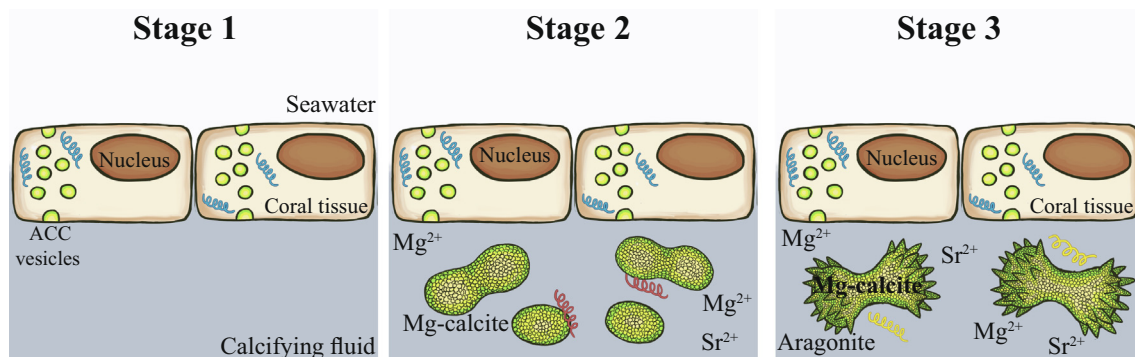

Fig. 8. Three-stage model of skeletogenesis in primary polyps. During the first stage, ion rich vesicles of ACC represented by green spheres, are formed in the tissue, in the presence of macro-molecules such as CARPs. In the second stage, the vesicles are transferred to the extracellular calcifying fluid, and Mg-Calcite rods/pristine dumbbells structures are deposited in the presence of CARPs. During the third stage, aragonite crystals are formed on top of the Mg-Calcite rods/dumbbells, which serve as seeds for the needle shaped crystal growth in a spherulitic growth pattern. The distinct CARPs, represented by helical structures (blue, red and yellow), play different roles in the biological precipitation the $CaCO_3$ minerals.

5. Conclusions

Based on our findings, we propose the following three-stage mineral formation model in primary polyps (Fig. 8): I) in addition to calcium transport channels [12–14] we suggest the formation of intracellular mineral vesicles. II) Formation of rod/dumbbell-shaped structures made of Mg-calcite, and III) formation of aragonite crystals. At stage I: divalent ion rich vesicles, likely containing amorphous material are formed within the cells. The origin of the divalent ions is likely from endocytosis of seawater [7,15] as the vesicles are stained by the membrane-impermeable calcein stain. We postulate that macro-molecules such as CARPs are present in these vesicles and induce the formation of transient ACC [90]. The vesicles deliver the mineral precursors into the calcifying fluid where it crystalizes into either Mg-calcite or aragonite as described in stage II and III.

Stage II: Formation of Mg-calcite CoCs. Initial deposition of skeletal mineral is in the form of Mg-calcite pristine dumbbells in *S. pistillata* or rod-shaped particles in *P. acuta*. Evidence shows [8] the presence of Mg-ACC in primary polyps, which we suggest is a precursor mineral for the Mg-calcite CoCs. The amorphous mineral however crystallizes rapidly in the calcifying fluid, as suggested by the birefringence of the pristine dumbbells in PLM under native conditions. The exact mechanism of the Mg-calcite rods/-dumbbells precipitation is still unknown, but it likely involves CARPs and possibly other specific organic macro-molecule [47,86,91].

Stage III: The third stage in the process is the large-scale buildup of aragonite crystals to fill the space between CoCs (dumbbell/rod) with needle-shaped fibers. Growing on top of the pristine dumbbell/rod structures (Figs. 1 and 2, Supplementary Movies 1–3). These aragonite crystals are the most ordered material in the growing coral, and as they accumulate, they become the most abundant mineral material in the coral. We suggest that aragonite is formed from a second precursor phase that transforms to aragonite via ACC and pAra phases [15].

The three-stage cycle repeats itself at different times and locations to form the basal plate and the septa. When these are well developed, mineral formation proceeds in the vertical direction in a precisely biological controlled process.

6. Data availability

The authors declare that the main data supporting the findings of this study are available within the article and its Supplementary Information files. Extra data are available from the corresponding author upon request.

Declaration of Competing Interest

The authors declare no competing financial interest.

Acknowledgements

Funding

Author contributions

M.N, A.A., I.P., P.P.L, D.A, and T.M. carried out the experiments, participated in the data analysis, participated in the design of the study and drafted the manuscript; M.N. carried out the field work, SEM imaging and EDS analysis; M.N, P.P.L and T.M microscopy imaging; I.P., M.N and T.M. carried out the Raman measurement and analysis; M.N, T.M, I.P, Y.P, and M.A, carried out the XRD and XRF measurements; M.N, O.S and Y.P carried out the XRD and XRF data analysis: A.A. and T.M. carried out the cryo-SEM imaging; D.A carried out the image analysis. All authors gave their final approval for publication.

Appendix A. Supplementary data

Supplementary data to this article can be found online at https://doi.org/10.1016/j.actbio.2019.07.016.

References

[1] W.J. Schmidt, Die Bausteine des Tierkorpers in Polarisiertem Lichte, Verlag, Bonn, 1924.

[2] H. Lowenstam, Minerals formed by organisms, Science 211 (4487) (1981) 1126–1131.

[3] G.D. Stanley, The evolution of modern corals and their early history, Earth-Sci. Rev. 60 (3–4) (2003) 195–225.

[4] J.D. Milliman, A.W. Droxler, Neritic and pelagic carbonate sedimentation in the marine environment: ignorance is not bliss, Geol. Rundsch. 85 (3) (1996) 496–504.

[5] A.L. Cohen, T.A. McConnaughey, Geochemical perspectives on coral mineralization, in: P.M. Dove, S. Weiner, J. DeYoreo (Eds.), Biomineralization, 2003, pp. 151–187.

[6] J.P. Cuif, Y. Dauphin, The environment recording unit in coral skeletons - a synthesis of structural and chemical evidences for a biochemically driven, stepping-growth process in fibres, Biogeosciences 2 (1) (2005) 61–73.

[7] P.L. Clode, A.T. Marshall, Low temperature FESEM of the calcifying interface of a scleractinian coral, Tissue Cell 34 (2002) 187–198.

[8] A. Akiva, M. Neder, K. Kahil, R. Gavriel, I. Pinkas, G. Goobes, T. Mass, Minerals in the pre-settled coral *Stylophora pistillata* crystallize via protein and ion changes, Nat. Commun. 9 (1) (2018) 1880.

[9] D. Allemand, É. Tambutté, D. Zoccola, S. Tambutté, Coral calcification, cells to reefs, in: Z. Dubinsky, N. Stambler (Eds.), Coral Reefs: An Ecosystem in Transition, Springer, New York, 2011, pp. 119–150.

[10] M.E. Barron, A.B. Thies, J.A. Espinoza, K.L. Barott, A. Hamdoun, M. Tresguerres, A vesicular Na+/Ca2+ exchanger in coral calcifying cells, PLoS One 13 (10) (2018) e0205367.

[11] T. Mass, J.L. Drake, E.C. Peters, W. Jiang, P.G. Falkowski, Immunolocalization of skeletal matrix proteins in tissue and mineral of the coral Stylophora pistillata, Proc. Natl. Acad. Sci. USA 111 (35) (2014) 12728–12733.

[12] D.S. Sevilgen, A.A. Venn, M.Y. Hu, E. Tambutté, D. de Beer, V. Planas-Bielsa, S. Tambutté, Full in vivo characterization of carbonate chemistry at the site of calcification in corals, Sci. Adv. 5 (1) (2019) eaau7447, https://doi.org/10.1126/sciadv.aau7447.

[13] D. Zoccola, E. Tambutte, F. Senegas-Balas, J.F. Michiels, J.P. Failla, J. Jaubert, D. Allemand, Cloning of a calcium channel alpha 1 subunit from the reef-building coral, Stylophora pistillata, Gene 227 (2) (1999) 157–167.

[14] D. Zoccola, E. Tambutte, E. Kulhanek, S. Puverel, J.C. Scimeca, D. Allemand, S. Tambutte, Molecular cloning and localization of a PMCA P-type calcium ATPase from the coral Stylophora pistillata, Biochim. Biophys. Acta Biomembr. 1663 (1–2) (2004) 117–126.

[15] T. Mass, A.J. Giuffre, C.-Y. Sun, C.A. Stifler, M.J. Frazier, M. Neder, N. Tamura, C. V. Stan, M.A. Marcus, P.U.P.A. Gilbert, Amorphous calcium carbonate particles form coral skeletons, Proc. Natl. Acad. Sci. USA 114 (37) (2017) E7670–E7678.

[16] E. Tambutte, S. Tambutte, N. Segonds, D. Zoccola, A.A. Venn, J. Erez, D. Allemand, Calcein labelling and electrophysiology: insights on coral tissue permeability and calcification, Proc. R. Soc. Lond. B 279 (2012) 19–27.

[17] N.I. Goreau, T.J. Goreau, R.L. Hayes, Settling, survivorship and spatial aggregation in planulae and juveniles of the coral *Porites Porites* (Pallas), Bull. Mar. Sci. 31 (2) (1981) 424–435.

[18] P.L. Harrison, Sexual reproduction of scleractinian corals, in: Z. Dubinsky, N. Stambler (Eds.), Coral Reefs: An Ecosystem in Transition, Springer, Netherlands, Dordrecht, 2011, pp. 59–85.

[19] J.H. Vandermeulen, Studies on reef corals. III. Fine structural changes of calicoblast cells in *Pocillopora damicornis* during settling and calcification, Mar. Biol. 31 (1) (1975) 69–77.

[20] J.-P. Cuif, Y. Dauphin, Microstructural and physico-chemical characterization of 'centers of calcification' in septa of some recent scleractinian corals, Paläontol. Z. 72 (3–4) (1998) 257–269.

[21] E.H. Gladfelter, Skeletal development in *Acropora cervicornis*, Coral Reefs 3 (1) (1984) 51–57.

[22] J. Stolarski, Three-dimensional micro- and nanostructural characteristics of the scleractinian coral skeleton: A Biocalcification proxy, Acta Palaeontologica Polonica 48 (3) (2003) 497–530.

[23] S. Von Euw, Q. Zhang, V. Manichev, N. Murali, J. Gross, L.C. Feldman, T. Gustafsson, C. Flach, R. Mendelsohn, P.G. Falkowski, Biological control of aragonite formation in stony corals, Science 356 (6341) (2017) 933–938.

[24] R.T. DeVol, C.-Y. Sun, M.A. Marcus, S.N. Coppersmith, S.C.B. Myneni, P.U.P.A. Gilbert, Nanoscale transforming mineral phases in fresh nacre, J. Am. Chem. Soc. 137 (41) (2015) 13325–13333.

[25] A. Meibom, J.P. Cuif, F.O. Hillion, B.R. Constantz, A. Juillet-Leclerc, Y. Dauphin, T. Watanabe, R.B. Dunbar, Distribution of magnesium in coral skeleton, Geophys. Res. Lett. 31 (23) (2004).

[26] K. Atoda, The larva and postlarval development of some reef-building corals. II. *Stylophora pistillata* (Esper), Sci. Rep. Tohoku Univ Ser 7 (4) (1947) 48–64.

[27] M. Gilis, A. Meibom, I. Domart-Coulon, O. Grauby, J. Stolarski, A. Baronnet, Biomineralization in newly settled recruits of the scleractinian coral *Pocillopora damicornis*, J. Morphol. 275 (12) (2014) 1349–1365.

[28] M. Raz-Bahat, J. Erez, B. Rinkevich, In vivo light-microscopic documentation for primary calcification processes in the hermatypic coral *Stylophora pistillata*, Cell Tissue Res. 325 (2) (2006) 361–368.

[29] Y. Ohno, A. Iguchi, C. Shinzato, M. Gushi, M. Inoue, A. Suzuki, K. Sakai, T. Nakamura, Calcification process dynamics in coral primary polyps as observed using a calcein incubation method, Biochem. Biophys. Rep. 9 (2017) 289–294.

[30] A. Venn, E. Tambutte, M. Holcomb, D. Allemand, S. Tambutte, Live tissue imaging shows reef corals elevate pH under their calcifying tissue relative to seawater, PLoS One 6 (5) (2011) e20013.

[31] C. Pan, D. Fang, G. Xu, J. Liang, G. Zhang, H. Wang, L. Xie, R. Zhang, A novel acidic matrix protein, PfN44, stabilizes magnesium calcite to inhibit the crystallization of aragonite, J. Biol. Chem. 289 (5) (2014) 2776–2787.

[32] S. Raz, S. Weiner, L. Addadi, Formation of high-magnesian calcites via an amorphous precursor phase: Possible biological implications, Adv. Mater. 12 (1) (2000) 38–42.

[33] R. Given, B.H. Wilkinson, Kinetic control of morphology, composition, and mineralogy of abiotic sedimentary carbonates, J. Sediment. Res. 55 (1) (1985) 109–119.

[34] Y. Kitano, D.W. Hood, Calcium carbonate crystal forms formed from sea water by inorganic processes, J. Oceanogr. Soc. Jpn. 18 (3) (1962) 141–145.

[35] T. Chen, J. Li, P. Shi, Y. Li, J. Lei, J. Zhou, Z. Hu, T. Duan, Y. Tang, W. Zhu, Effects of montmorillonite on the mineralization and cementing properties of microbiologically induced calcium carbonate, Adv. Mater. Sci. Eng. 2017 (2017) 13.

[36] A. Sánchez-Navas, A. Martín-Algarra, M.A. Rivadeneyra, S. Melchor, J.D. Martín-Ramos, Crystal-growth behavior in Ca–Mg carbonate bacterial spherulites, Cryst. Growth Des. 9 (6) (2009) 2690–2699.

[37] C. Zhang, F. Li, J. Lv, Morphology and formation mechanism in precipitation of calcite induced by Curvibacter lanceolatus strain HJ-1, J. Cryst. Growth 478 (2017) 96–101.

[38] Z.A. Al Disi, S. Jaoua, T.R.R. Bontognali, E.S.M. Attia, H.A.A.S. Al-Kuwari, N. Zouari, Evidence of a role for aerobic bacteria in high magnesium carbonate formation in the evaporitic environment of dohat faishakh sabkha in Qatar, Front. Environ. Sci. 5 (1) (2017).

[39] Y. Shlesinger, T.L. Goulet, Y. Loya, Reproductive patterns of scleractinian corals in the northern Red Sea, Mar. Biol. 132 (4) (1998) 691–701.

[40] J. Schindelin, I. Arganda-Carreras, E. Frise, V. Kaynig, M. Longair, T. Pietzsch, S. Preibisch, C. Rueden, S. Saalfeld, B. Schmid, J.-Y. Tinevez, D.J. White, V. Hartenstein, K. Eliceiri, P. Tomancak, A. Cardona, Fiji: an open-source platform for biological-image analysis, Nat. Methods 9 (7) (2012) 676–682.

[41] T. Mass, H.M. Putnam, J.L. Drake, E. Zelzion, R.D. Gates, D. Bhattacharya, P.G. Falkowski, Temporal and spatial expression patterns of biomineralization proteins during early development in the stony coral *Pocillopora damicornis*, Proc. R. Soc. B 283 (1829) (2016) 20160322, https://doi.org/10.1098/rspb.2016.0322.

[42] M. Martin, Cutadapt removes adapter sequences from high-throughput sequencing reads, 17(1) (2011) 3

[43] J.L. Drake, T. Mass, L. Haramaty, E. Zelzion, D. Bhattacharya, P.G. Falkowski, Proteomic analysis of skeletal organic matrix from the stony coral *Stylophora pistillata*, Proc. Natl. Acad. Sci. USA 110 (10) (2013) 3788–3793.

[44] A. Dobin, C.A. Davis, F. Schlesinger, J. Drenkow, C. Zaleski, S. Jha, P. Batut, M. Chaisson, T.R. Gingeras, STAR: ultrafast universal RNA-seq aligner, Bioinformatics (Oxford, England) 29 (1) (2013) 15–21.

[45] S. Anders, P.T. Pyl, W. Huber, HTSeq–a Python framework to work with high-throughput sequencing data, Bioinformatics (Oxford, England) 31 (2) (2015) 166–169.

[46] https://bioconductor.org/packages/release/bioc/html/DESeq2.html.

[47] R. Gavriel, M. Nadav-Tsubery, Y. Glick, A. Yarmolenko, R. Kofman, K. Keinan-Adamsky, A. Berman, T. Mass, G. Goobes, The coral protein CARP3 acts from a disordered mineral surface film to divert aragonite crystallization in favor of Mg-Calcite, Adv. Funct. Mater. 28 (21) (2018) 1707321.

[48] V. Zizak, The mySpot beamline at BESSY II, J. Large Scale Res. Facil. 2 (2016) A102.

[49] G. Benecke, W. Wagermaier, C. Li, M. Schwartzkopf, G. Flucke, R. Hoerth, I. Zizak, M. Burghammer, E. Metwalli, P. Müller-Buschbaum, M. Trebbin, S. Förster, O. Paris, S.V. Roth, P. Fratzl, A customizable software for fast reduction and analysis of large X-ray scattering data sets: applications of the new DPDAK package to small-angle X-ray scattering and grazing-incidence small-angle X-ray scattering, J. Appl. Crystallogr. 47 (Pt 5) (2014) 1797–1803.

[50] Origin. 2003. Origin 7.5. OriginLab Corp., Northampton, MA.

[51] V.A. Solé, E. Papillon, M. Cotte, P. Walter, J. Susini, A multiplatform code for the analysis of energy-dispersive X-ray fluorescence spectra, Spectrochim. Acta, Part B 62 (1) (2007) 63–68.

[52] B. Obara, A. Jabeen, N. Fernandez, P.P. Laissue, A novel method for quantified, superresolved, three-dimensional colocalisation of isotropic, fluorescent particles, Histochem. Cell Biol. 139 (3) (2013) 391–402.

[53] H. Zhao, Biomineralization of calcium and magnesium carbonate minerals induced by Bacillus licheniformis and its application in water softening, 2017

[54] O. Braissant, G. Cailleau, C. Dupraz, E.P. Verrecchia, Bacterially induced mineralization of calcium carbonate in terrestrial environments: the role of exopolysaccharides and amino acids, J. Sediment. Res. 73 (3) (2003) 485–490.

[55] M.A. Rivadeneyra, A. Martín-Algarra, A. Sánchez-Navas, D. Martíin-Ramos, Carbonate and phosphate precipitation by Chromohalobacter marismortui, Geomicrobiol J. 23 (2) (2006) 89–101.

[56] Z.L. Han, D., H. Yan, P. Li, Biomineralization of carbonate minerals induced by halophilic Chromohalobacter israelensis in high salt concentration: implications for natural environments, Preprints 2017030043 (2017).

[57] M.A.A. Rivadeneyra, G. Delgado, M. Soriano, A. Ramos-Cormenzana, R. Delgado, Precipitation of carbonates by Nesterenkonia halobia in liquid media, Chemosphere 41 (4) (2000) 617–624.

[58] G. Mor Khalifa, K. Kahil, J. Erez, I. Kaplan Ashiri, E. Shimoni, I. Pinkas, L. Addadi, S. Weiner, Characterization of unusual MgCa particles involved in the formation of foraminifera shells using a novel quantitative cryo SEM/EDS protocol, Acta Biomater. 77 (2018) 342–351.

[59] R. Frech, E.C. Wang, J.B. Bates, The i.r. and Raman spectra of CaCO$_3$ (aragonite), Spectrochim. Acta Part A Mol. Biomol. Spectrosc. 36 (10) (1980) 915–919.

[60] M. De La Pierre, C. Carteret, L. Maschio, A. André, R. Orlando, R. Dovesi, The Raman spectrum of CaCO$_3$ polymorphs calcite and aragonite: a combined experimental and computational study, J. Chem. Phys. 140 (16) (2014) 164509.

[61] J. Perrin, D. Vielzeuf, D. Laporte, A. Ricolleau, G.R. Rossman, N. Floquet, Raman characterization of synthetic magnesian calcites, Am. Mineral. 101 (11) (2016) 2525–2538.

[62] K.E. Chave, A solid solution between calcite and dolomite, J. Geol. 60 (2) (1952) 190–192.

[63] E. Zolotoyabko, E.N. Caspi, J.S. Fieramosca, R.B. Von Dreele, F. Marin, G. Mor, L. Addadi, S. Weiner, Y. Politi, Differences between bond lengths in biogenic and geological calcite, Cryst. Growth Des. 10 (3) (2010) 1207–1214.

[64] M. Albéric, E.N. Caspi, M. Bennet, W. Ajili, N. Nassif, T. Azaïs, A. Berner, P. Fratzl, E. Zolotoyabko, L. Bertinetti, Y. Politi, Interplay between calcite, amorphous calcium carbonate, and intracrystalline organics in sea urchin skeletal elements, Cryst. Growth Des. 18 (4) (2018) 2189–2201.

[65] H.A. Lowenstam, Factors affecting the aragonite: calcite ratios in carbonate-secreting marine organisms, J. Geol. 62 (3) (1954) 284–322.

[66] E.H. Gladfelter, Skeletal development in *Acropora cervicornis*. Diel patterns of calcium carbonate accretion, Coral Reefs 2 (1983) 91–100.

[67] E. Gladfelter, Skeletal development in Acropora cervicornis II: Diel patterns of calcium carbonate accretion, Coral Reefs 2 (1983) 91–100.

[68] B.R. Constantz, A. Meike, Calcite centers of calcification in Mussa angulosa (Scleractinia), in: R.E. Crick (Ed.), Origin, Evolution and Modern Aspects of Biomineralization in Plants and Animals, Plenum Press, New York, 1989, pp. 201–208.

[69] J.E. Houck, R.W. Buddemeier, K.E. Chave, Skeletal low-magnesium calcite in living scleractinian corals, Science 189 (4207) (1975) 997.

[70] J.H. Vandermeulen, N. Watabe, Studies on reef corals. I. Skeleton formation by newly settled planula larva of *Pocillopora damicornis*, Mar. Biol. 23 (1973) 47–57.

[71] S. Goffredo, E. Caroselli, F. Mezzo, L. Laiolo, P. Vergni, L. Pasquini, O. Levy, F. Zaccanti, A. Tribollet, Z. Dubinsky, G. Falini, The puzzling presence of calcite in skeletons of modern solitary corals from the Mediterranean Sea, Geochim. Cosmochim. Acta 85 (2012) 187–199.

[72] C.-Y. Sun, M.A. Marcus, M.J. Frazier, A.J. Giuffre, T. Mass, P.U.P.A. Gilbert, Spherulitic growth of coral skeletons and synthetic aragonite: nature's three-dimensional printing, ACS Nano 11 (7) (2017) 6612–6622.

[73] M.M. Ogilvie III, Microscopic and systematic study of madreporarian types of corals, Philos. Trans. R. Soc. London, Ser. B 187 (1896) 83–345.

[74] L. Gránásy, T. Pusztai, G. Tegze, J.A. Warren, J.F. Douglas, Growth and form of spherulites, Phys. Rev. E 72 (1) (2005) 011605.

[75] A. Gal, K. Kahil, N. Vidavsky, R.T. DeVol, P.U.P.A. Gilbert, P. Fratzl, S. Weiner, L. Addadi, Particle accretion mechanism underlies biological crystal growth from an amorphous precursor phase, Adv. Funct. Mater. 24 (34) (2014) 5420–5426.

[76] A. Shechter, L. Glazer, S. Cheled, E. Mor, S. Weil, A. Berman, S. Bentov, E.D. Aflalo, I. Khalaila, A. Sagi, A gastrolith protein serving a dual role in the formation of an amorphous mineral containing extracellular matrix, Proc. Natl. Acad. Sci. USA 105 (20) (2008) 7129–7134.

[77] E. Beniash, J. Aizenberg, L. Addadi, S. Weiner, Amorphous calcium carbonate transforms into calcite during sea urchin larval spicule growth, Proc. R. Soc. Lond. B: Biol. Sci. 264 (1380) (1997) 461–465.

[78] Y. Politi, R.A. Metzler, M. Abrecht, B. Gilbert, F.H. Wilt, I. Sagi, L. Addadi, S. Weiner, P.U.P.A. Gilbert, Transformation mechanism of amorphous calcium carbonate into calcite in the sea urchin larval spicule, Proc. Natl. Acad. Sci. USA 105 (45) (2008) 17362–17366.

[79] J.P.R. De Villiers, Crystal Structures of Aragonite, Strontianite, and Witherite, Am. Mineral. 56 (5–6) (1971) 758–767.

[80] Z.Y. Li, W.M. Lam, C. Yang, B. Xu, G.X. Ni, S.A. Abbah, K.M.C. Cheung, K.D.K. Luk, W.W. Lu, Chemical composition, crystal size and lattice structural changes after incorporation of strontium into biomimetic apatite, Biomaterials 28 (7) (2007) 1452–1460.

[81] Y. Isa, An electron microscope study on the mineralization of the skeleton of the staghorn coral *Acropora hebes*, Mar. Biol. 93 (1) (1986) 91–101.

[82] A.T. Marshall, P.L. Clode, R. Russell, K. Prince, R. Stern, Electron and ion microprobe analysis of calcium distribution and transport in coral tissues, J. Exp. Biol. 210 (14) (2007) 2453–2463.

[83] T. Takeuchi, L. Yamada, C. Shinzato, H. Sawada, N. Satoh, Stepwise evolution of coral biomineralization revealed with genome-wide proteomics and transcriptomics, PLoS One 11 (6) (2016) e0156424.

[84] R. Liu, X. Xu, Y. Cai, A. Cai, H. Pan, R. Tang, K. Cho, Preparation of calcite and aragonite complex layer materials inspired from biomineralization, Cryst. Growth Des. 9 (7) (2009) 3095–3099.

[85] T. Mass, J.L. Drake, J.M. Heddleston, P.G. Falkowski, Nanoscale visualization of biomineral formation in coral proto-polyps, Curr. Biol. 27 (20) (2017) 3191–3196.e3.

[86] M. Reggi, S. Fermani, V. Landi, F. Sparla, E. Caroselli, F. Gizzi, Z. Dubinsky, O. Levy, J.-P. Cuif, Y. Dauphin, S. Goffredo, G. Falini, Biomineralization in Mediterranean corals: the role of the intraskeletal organic matrix, Cryst. Growth Des. 14 (9) (2014) 4310–4320.

[87] J.P. Cuif, Y. Dauphin, J. Doucet, M. Salome, J. Susini, XANES mapping of organic sulfate in three scleractinian coral skeletons, Geochim. Cosmochim. Acta 67 (1) (2003) 75–83.

[88] J.P. Cuif, Y. Dauphin, B. Farre, G. Nehrke, J. Nouet, M. Salome, Distribution of sulphated polysaccharides within calcareous biominerals suggests a widely shared two-step crystallization process for the microstructural growth units, Mineral. Mag. 72 (1) (2008) 233–237.

[89] G. Falini, S. Fermani, Nucleation and growth from a biomineralization perspective, in: A.E.S. Van Driessche, M. Kellermeier, L.G. Benning, D. Gebauer (Eds.), New Perspectives on Mineral Nucleation and Growth: From Solution Precursors to Solid Materials, Springer International Publishing, Cham, 2017, pp. 185–197.

[90] J. Aizenberg, L. Addadi, S. Weiner, G. Lambert, Stabilization of amorphous calcium carbonate by specialized macromolecules in biological and synthetic precipitates, Adv. Mater. 8 (3) (1996) 222–226.

[91] G. Falini, M. Reggi, S. Fermani, F. Sparla, S. Goffredo, Z. Dubinsky, O. Levi, Y. Dauphin, J.-P. Cuif, Control of aragonite deposition in colonial corals by intra-skeletal macromolecules, J. Struct. Biol. (2013).